

Characterization of the Hamamatsu R11780 12 inch Photomultiplier Tube

J. Brack^d, B. Delgado^a, J. Dhooghe^e, J. Felde^e, B. Gookin^d, S. Grullon^{a,*}, J.R. Klein^a,
R. Knapik^b, A. LaTorre^c, S. Seibert^a, K. Shapiro^a, R. Svoboda^e, L. Ware^a, R. Van Berg^a

^aUniversity of Pennsylvania, Philadelphia, PA 19104, USA

^bNorwich University, Northfeild, VT 05663, USA

^cUniversity of Chicago, Chicago, IL 60637, USA

^dColorado State University, Fort Collins, CO 80523, USA

^eUniversity of California, Davis, Davis, CA 95616, USA

Abstract

Future large water Cherenkov and scintillator detectors have been proposed for measurements of long baseline neutrino oscillations, proton decay, supernova and solar neutrinos. To ensure cost-effectiveness and optimize scientific reach, one of the critical requirements for such detectors are large-area, high performance photomultiplier tubes (PMTs). One candidate for such a device is the Hamamatsu R11780, a 12" PMT that is available in both standard and high quantum efficiency versions. Measurements of the single photoelectron response characteristics, relative efficiencies of the standard and high quantum efficiency versions, a preliminary measurement of the absolute quantum efficiency of the standard quantum efficiency version, and a two-dimensional scan of the relative efficiency across the photocathode surface are presented in this paper. All single photoelectron investigations were made using a Cherenkov light source at room temperature at a gain of 1×10^7 . These results show that the R11780 PMT is an excellent candidate for such large optical detectors.

Keywords: Photomultiplier tube, neutrino detectors, optical detectors, photon detection, single phase dark matter

1. Introduction

Great discoveries in neutrino physics have been made with large, monolithic, optical detectors. The Super-Kamiokande (Super-K) 40 ktonne water Cherenkov detector discovered unambiguous evidence of atmospheric neutrino oscillations [1], the Sudbury Neutrino Observatory (SNO) solved the long-standing solar neutrino problem using a 1 ktonne heavy-water Cherenkov detector [2] and the KamLAND ~ 1 ktonne liquid scintillator detector observed the same oscillation terrestrially with reactor antineutrinos. Recently the RENO [3] and Daya Bay [4] liquid scintillator detectors have made definitive measurements of the third neutrino mixing angle. In each of these experiments, the performance of large-area photomultiplier tubes (PMTs) was critical to ensure large scientific reach at reasonable cost.

*Corresponding author

Email address: grullons@hep.upenn.edu (S. Grullon)

Preprint submitted to Nuclear Instruments And Methods A

February 21, 2022

It is likely that further progress in neutrino physics can be made using large water or liquid scintillator detectors, and several proposals for such detectors have been put forward [5, 6, 7, 8]. In addition, searches for proton decay either via $p \rightarrow e^+\pi^0$ or, possibly with scintillator or loading with Gd [9], $p \rightarrow K^+\bar{\nu}$, as well as studies of atmospheric neutrinos including searches for non-standard interactions, solar neutrinos including observation of the Day/Night asymmetry [10], and possibly even, in loaded scintillator, searches for neutrinoless double beta decay (following the SNO+ [11] and KamLAND-Zen [12]) can be done with very large masses observed by efficient, inexpensive PMTs. The IceCube Neutrino Observatory [13] consists of a kilometer-cubed instrumented volume of glacial ice at the South Pole with well-tested large area 10-inch PMTs [14]. Very large-scale ‘single-phase’ dark matter detectors [15] have also been proposed that use the same principle.

Typically, the physics reach of such detectors is optimized by increasing the number of detected photons, narrowing the resolution for photon arrival times, and being able to distinguish single photons from multiple photons. These general requirements argue for a very large number of PMTs with excellent timing and charge response. Maintaining a reasonable cost, however, argues for reducing the total number of channels, by using the largest-area phototubes that can withstand the environment (e.g., pressure and temperature within the detector volume), and by increasing the efficiency of each PMT.

The 12-inch Hamamatsu R11780 is an excellent candidate for such large detectors based on its large size, the existence of a high quantum efficiency (HQE) design, and a mechanical construction that can withstand high water pressures [16]. We describe here measurements characterizing the single photoelectron response of both the standard and high quantum efficiency versions of the Hamamatsu R11780 PMT. Section 2 describes the Hamamatsu R11780 PMT and describes magnetic field effects on the PMT response. Section 3 describes the experimental setup used for the single photoelectron characterization. We describe the results of the charge and time characterization of the R11780 PMT in Section 4.1 and Section 4.2, respectively, a measurement made of the absolute quantum efficiency in Section 4.4, and describe the position dependence along the photocathode of the detection efficiency and timing response in Section 4.6.

2. The R11780 PMT

The R11780 PMT developed by Hamamatsu Photonics (Figure 1) has a 12” diameter photocathode, and ten linear-focused dynode stages. We tested two sets of phototubes: “standard quantum efficiency” (SQE) tubes with quantum efficiencies anticipated to peak near 21% at 390 nm, and bialkali “high quantum efficiency” (HQE) tubes with quantum efficiencies peaking around 32% at 390 nm. We note that the anticipated peak quantum efficiency of the standard configuration is lower than the average peak quantum efficiency for the Hamamatsu 10-inch R7081 PMT, which is typically 25% [14], and that the anticipated peak quantum efficiency of the high quantum efficiency configuration is the same as the average peak quantum efficiency for the high quantum efficiency configuration of the Hamamatsu R7081 PMT of 32% at 390 nm [8].

2.1. Measurement of Effects due to Magnetic Fields

It is well known that the electron focusing capabilities of a PMT are affected by magnetic fields. The Lorentz force felt by the electron implies that a field transverse to the PMT will tend to deflect some fraction of electrons away from the first dynode,

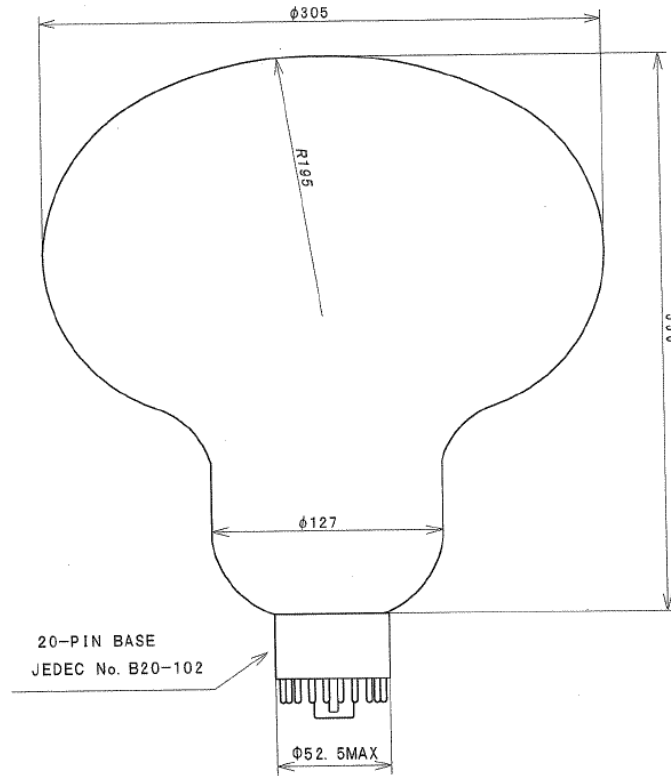


Figure 1: The R11780 12 inch Hamamatsu PMT and the two-cable voltage divider used. The two-cable voltage divider was designed to be cathode-grounded, and the coupling capacitor required to separate the signal from the positive high voltage was included for convenience.

thereby reducing the PMT's collection efficiency [17]. Tests to investigate the magnitude of this effect were done for one R11780 high quantum efficiency PMT in a tunable, tri-axial, magnetic field environment at the University of California, Davis. Three pairs of 1 m^2 copper Helmholtz coils, separated by 0.5 m, were arranged along perpendicular axes inside a dark room. Each coil pair was connected in series, and a variable DC current, capable of producing fields of $\sim 500 \text{ mG}$ (similar to the magnitude of the Earth's magnetic field), was driven through each. The uniformity of the field was measured to be $\pm 10 \text{ mG}$ within a 12" cube around the PMT bulb. This non-uniformity is primarily caused by

variations in the Earth's magnetic field inside the laboratory.

During testing it was discovered that the R11780's purchased were constructed with a metal tab of considerable magnetization affixed to the outer base of the dynode stack. This magnetization is localized, but does introduce some field non-uniformity within the PMT. The fields are measured at the location of the center of the PMT prior to placing the PMT inside the coils to accurately simulate external field values.

Testing was carried out by initially canceling the vertical component of the Earth's magnetic field, and then varying independently the field strength in both transverse directions. For these studies, the PMT was supported such that it was pointed upward, in the +Z direction. The +X direction is defined by the notch on the PMT's base connection, between the first and twentieth pins, and the +Y direction follows a right handed coordinate system convention. The light source used was a green (570 nm) LED positioned ~ 0.5 m above the PMT to fully illuminate the PMT face. Since the magnetic field affects the electron focusing, dependence on the photon wavelength is assumed to be small, and ultimately not easily mitigated by external means.

Data was acquired using a Tektronix DPO7254 digitizing oscilloscope. At each field value the individual PMT waveforms from 50,000 identical LED triggers are stored. The waveforms are integrated in software to remove small DC offsets, and obtain the average charge collected. During these tests the PMT was operated at a gain of 1×10^7 .

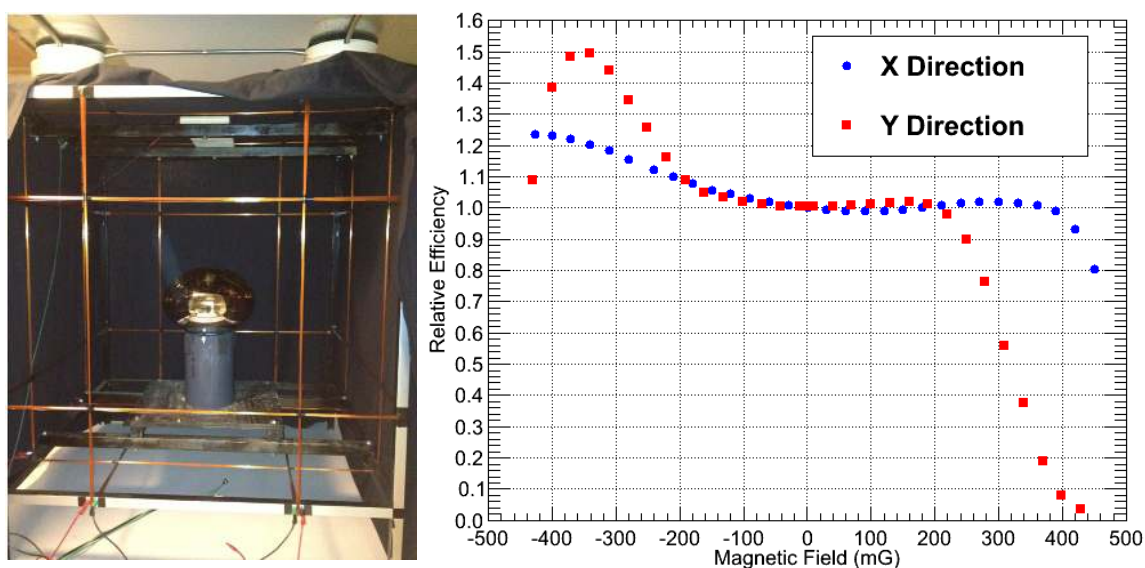


Figure 2: Left: Helmholtz coils and PMT testing setup at UC Davis. Right: Results of measured charge relative to zero field for a number of magnetic field strengths. During each test the opposite transverse field value is held at zero.

A fine scan was done for magnetic fields along X and Y between -450 mG and +450 mG. The data show an expected degradation of efficiency at fields along the +X and +Y directions, but an unexpected increase in efficiency for fields in the -X and -Y directions. One can see, however, that for fields greater than 500 mG the data appear to return to the expected behavior of decreasing efficiency. Although this behavior is unexpected, it can be understood that the PMT collection efficiency is not optimized with respect to this effect. It should be noted that these measurements can not be used to accurately predict the effect of a field along X and Y simultaneously, but the scale of the effect is well established by the data presented.

In a future large scale detector instrumented with R11780 PMTs, it is clear that mitigation of the Earth’s magnetic field is necessary. In some cases, simply orienting the PMT in an optimal way could be sufficient. To maximize PMT performance, it is usually desirable to either actively cancel the field with coils, or passively reduce the field using a high magnetic permeability metal surrounding parts of the PMT. These tests indicate that transverse fields $< \sim 200$ mG will have $< \sim 5\%$ degradation, and can even result in improved performance.

3. Single Photoelectron Characterization Experimental Setup

For a large-scale Cherenkov or scintillator experiment, the detector’s capability for discriminating different particle types, reconstructing particle positions and directions, and measuring energy deposition depends primarily on the performance of the chosen PMT. The PMTs in such large detectors typically detect no more than a few photons per event. Thus, the single photoelectron response is most important in determining the optimal PMT. A detailed characterization of this response is also critical for developing a complete model of the detector, useful both for understanding the detector’s response and for position, energy and direction reconstruction in the case of Cherenkov detectors.

Our measurements of the single photoelectron response of the Hamamatsu R11780 uses a simple Cherenkov light source. The Cherenkov source was constructed by embedding two $0.1 \mu\text{Ci}$ discs of ^{90}Sr in a piece of UV-transparent acrylic machined into an approximately 1 inch cube. The acrylic is the same material as was used in the acrylic vessel (the acrylic sheets were provided by PolyCast[®]) to hold the heavy water in the Sudbury Neutrino Observatory (SNO) experiment, and its optical properties have been already studied in great detail [18]. A 1-inch Hamamatsu R7600-200 super bialkali high quantum efficiency PMT is optically coupled with the acrylic source and is used as a fast (~ 250 ps FWHM) trigger as shown in Figure 3. The ^{90}Sr undergoes a 0.546 MeV β -

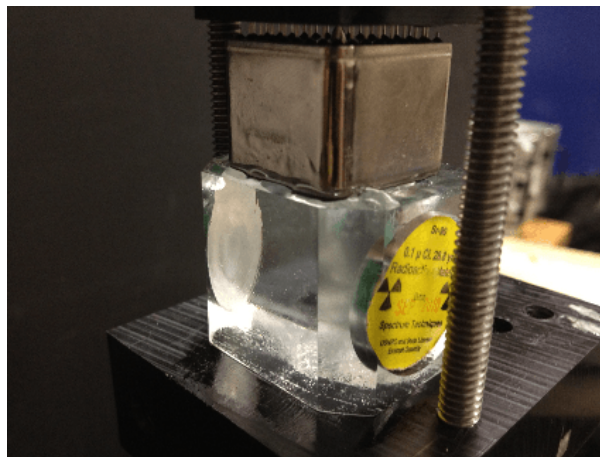


Figure 3: The Cherenkov light source. Two $0.1 \mu\text{Ci}$ ^{90}Sr discs are embedded on the side of a 1 inch cube, which is optically coupled to a 1 inch PMT on top of the acrylic that acts as a trigger.

decay into the yttrium isotope ^{90}Y with a half-life of 29.1 years. The ^{90}Y also undergoes a β - decay into ^{90}Zr (zirconium), which is stable. The half life for ^{90}Y is 64 hours and the emitted electron from the ^{90}Y decay has an energy 2.28 MeV which will enter the acrylic and will produce Cherenkov light.

The Cherenkov source has the advantage that its wavelength spectrum is broadband, nearly identical to a water Cherenkov detector and spanning the same range as a scintillation detector. The photons are produced with a very narrow time distribution, and thus allow precision measurements of the PMT timing response. With the PMTs placed 45 cm from the Cherenkov source, the fraction of coincidences between an individual PMT and the trigger PMT was $\sim 3\text{-}5\%$. Assuming the number distribution of photons incident on the PMT photocathode are Poisson distributed, we were predominantly in the single photoelectron regime. Nevertheless, there was a small contamination from multiple photons that are not described by Poisson statistics. This non-Poisson contribution of multiple photons is due to the correlated nature of Cherenkov light, cases where the Cherenkov cone points primarily toward the PMT and therefore is not a pure source of single photoelectrons. We have not made any corrections for that effect in the measurements we present here because the SPE characterization is insensitive to this effect. Section 4.7 shows this contamination is relatively small and only affects the high tail of the charge distribution.

A 2 m by 2 m by 0.9 m dark box (Figure 4) was built to house the Cherenkov light source along with the PMTs being tested. Our data acquisition system was a LeCroy Waverunner 6050A 500 MHz oscilloscope, running LeCrunch [19] software that allowed us to acquire full waveform data at rates up to 1 kHz. No additional amplification of the PMT signal was performed. Given the size of the dark box and the speed of our acquisition system, we were able to characterize up to 3 PMTs at a time, each optically isolated from one another. The entire dark box setup is surrounded by a set of Helmholtz coils to help reduce the effects of the vertical component of Earth’s magnetic field. After compensation, the magnetic field in the dark box has a upward z -component of less than 5 mG and residual components in the x and y directions of around 170 mG and 50 mG respectively. For some of our measurements, we also added Finemet[®] [20] shielding to the entire box, further reducing the x and y components of the field to 34 mG and 23 mG, respectively.

3.1. Data Acquisition and Storage

Full waveform traces were stored for both the trigger PMT and the PMTs being tested. Each trace consists of 1252 samples at 0.2 ns intervals for a total of 250.4 ns per trace. Figure 5 shows typical waveform traces in a coincident event for a R11780-SQE PMT.

The raw data were transferred to a data storage server in a custom HDF5 format. For a gain of 1×10^7 , 20 individual data runs were recorded to provide adequate statistics in the single photoelectron (SPE) analysis. A typical individual data run consisted of 100,000 triggered events which corresponded to $\sim 3000\text{-}5000$ coincident events per run. Analysis software processed the data immediately after the data runs were completed and the results were uploaded into a CouchDB database. With approximately 60,000 coincident pulses, the statistical uncertainties on most SPE parameters are at or below the 1% level and therefore were sufficient for most of the characterization. A CouchApp web-based application was created to make data publicly accessible [21] and the results were aggregated into easily accessible tables.



Figure 4: The dark box setup with Helmholtz coils for cancellation of the Earth's magnetic field. At a distance of 1.5 m, the coincidence rate is kept below 5%.

4. R11780 Single Photoelectron Characterization Results

4.1. R11780 Charge Response

Figure 6 shows typical SPE spectra for both the standard and high quantum efficiency R11780 PMT models. The data were taken using the triggered Cherenkov source. These spectra were created by integrating over a fixed 30 ns 'prompt' time window in each R11780 waveform for all triggered events.

The figures that demonstrate the SPE charge response of a PMT in this paper, such as Fig. 6, are broadly characterized by the convolution of two distributions. The first is a tall narrow distribution centered at 0.0 pC, which is the electronic noise inherent in the data acquisition system. The second is the actual SPE charge distribution with a peak at about 1.6 pC, which corresponds to a gain of 1×10^7 . The height of the SPE peak relative to the depth of the 'valley' between the SPE charge distribution and the electronic noise peak known as the 'pedestal' provides a metric for the PMT's ability to distinguish true photons from electronic noise. Real photons can occasionally produce very low charges and therefore the valley consists of both very low charges from photoelectrons and upward fluctuations of the electronic noise. A larger Peak-to-Valley ratio results in a lower percentage of low charge events and a higher overall detection efficiency for a given charge threshold. Some PMTs exhibit a unusually long tail near the high side of the charge spectrum. Some of the events in the high charge tail are from multiple photoelectrons and this is discussed in Section 4.7. The size of the high-charge tail coupled with the width of the charge distribution affects the PMT's ability to distinguish between single and two or more photons.

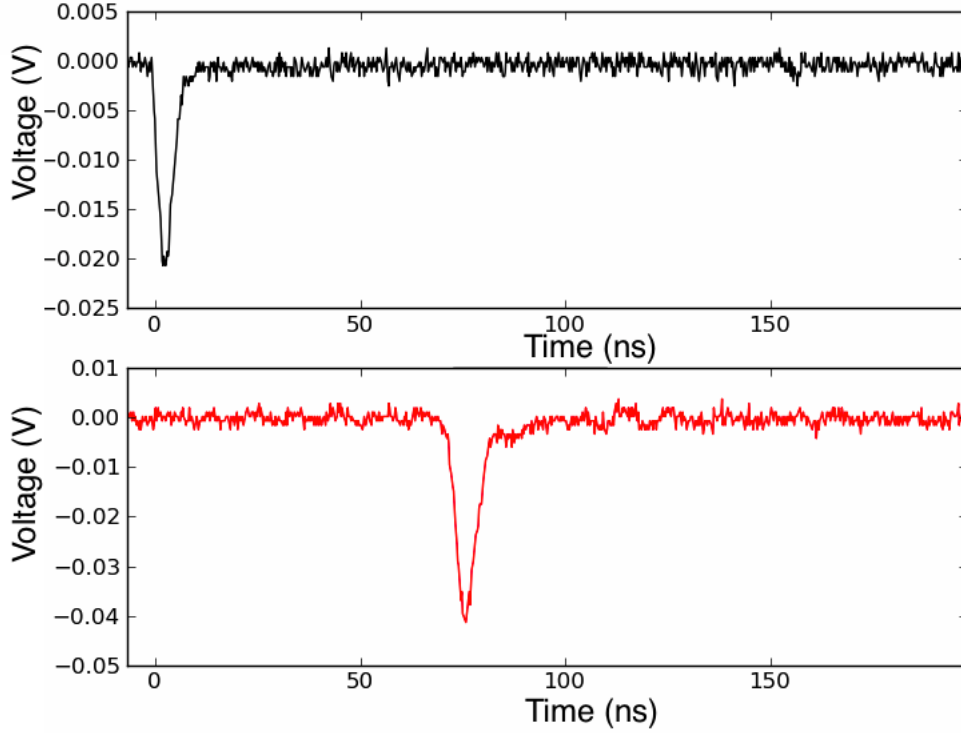


Figure 5: The entire trigger PMT digitized trace is displayed (top), as well as the trace for the R11780 PMT being characterized (bottom). The waveforms were used for both timing and charge. Due to the low coincidence rate, the majority of triggers recorded no pulse from the R11780 PMT.

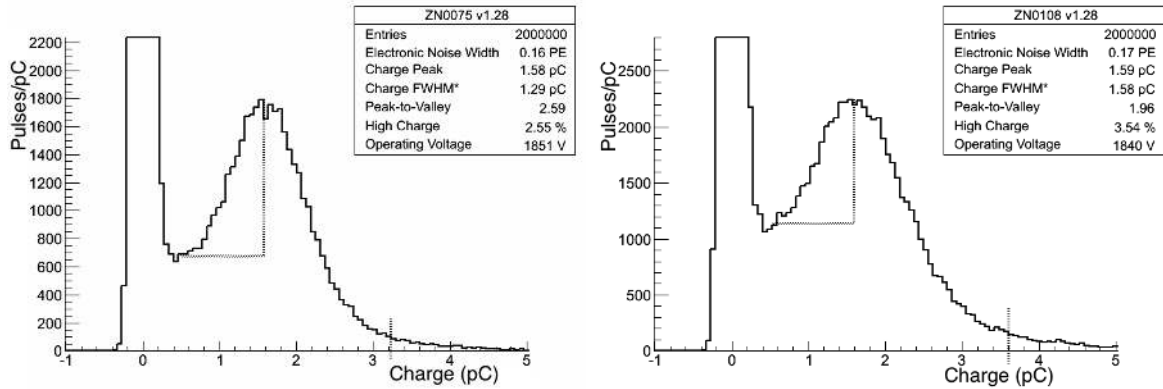


Figure 6: The single photoelectron spectrum for a Hamamatsu R11780 PMT. The left distribution is displayed for a standard quantum efficiency PMT and on the right is shown for the high quantum efficiency model. The events to the right of the dashed vertical line at ~ 3 pC represents the “high charge tail” of the distribution. The enhancement near 3.2 pC may be due to events with two photoelectrons. The high charge tails in the two distributions are higher than expected from Poisson statistics, for the reasons outlined in the text. The expected number of multiple photoelectron events from Poisson statistics for these examples is negligible since the coincidence rate for the left distribution is 1.2%, and the coincidence rate for the right distribution is 2.0% (which correspond to Poisson means of 0.012 and 0.02, respectively).

For each run, we perform several fits to the charge spectra to extract the SPE parameters. A Gaussian is fit to the electronic noise peak, another Gaussian is fit to the SPE

distribution and a third fit is used to locate the valley. While the SPE distribution generally has significant non-Gaussian tails, the Gaussian approximation is adequate near the peak of the distribution for the application of comparing the SPE response of different PMTs. The explicit definitions of the fit parameters are:

Electronic Noise Width: The Gaussian fit is done around the peak value (located near 0.0 pC) $\pm N_{half}$ bins, where N_{half} is the number of bins to the half height location on the positive side of the peak. The width is defined as the sigma from the fit (4 times this value is generally close to 1/4 PE discriminator threshold typically used in experiments).

Charge Peak: The Gaussian fit is centered on the SPE distribution peak, from $\frac{2}{3}\text{Max}_{SPE}$ to 1.5Max_{SPE} , where Max_{SPE} is the bin of maximum value in the integrated charge peak. The gain is defined as the ratio of the electron charge to the peak charge, thus a gain of 1.0×10^7 corresponds to a charge peak of 1.6 pC if no additional amplification is performed. Our test setup does not include an additional amplifier.

Charge FWHM: $2\sigma_{SPE}\sqrt{2\ln(2)}$ is the charge full width at half maximum value, where σ_{SPE} is the sigma from the Gaussian fit to the SPE distribution.

Peak/Valley: The height of the peak is defined by the overall normalization of the Gaussian fit to the SPE distribution. The height of the valley is found by fitting a quadratic from $6\sigma_{elec}$ to $\frac{2}{3}\text{Max}_{SPE}$, and the ratio is defined between the two.

High Charge Tail: We estimate any anomalously high charge tail by measuring the ratio of the number of events with a charge $3\sigma_{SPE}$ above the SPE peak to the total number above the electronic noise width (defined above). For our Cherenkov source, the high charge tail is non-trivially contaminated by multi-photoelectron events, and we do not correct for that effect here.

The results of our measurements of the single photoelectron charge response for standard quantum efficiency versions of the R11780 are shown in Table 1, and for the high quantum efficiency versions in Table 2. The results for the standard QE tubes are averaged over seven PMTs and the HQE results are averaged over ten PMTs. The data was taken at a gain of 1×10^7 for both configurations. As the tables show, the charge response of these tubes is very good overall compared to the 8-inch tubes used for SNO [18] and the 20-inch tubes used for Super Kamiokande [1]. We note again that the high charge tail has a non-trivial contribution from multi-photoelectrons due to the nature of our Cherenkov source and that the effect is bigger for the HQE PMTs due to their higher detection efficiency. We also note that the Peak/Valley ratio for the HQE PMTs appears to be systematically lower than for the standard quantum efficiency versions, although this difference is not inconsistent with PMT-to-PMT variations seen within each sample.

4.2. R11780 Timing Response

The transit time between the absorption of a photon at the photocathode and the output pulse from the anode of a PMT varies from photoelectron to photoelectron, and the inherent fluctuation in the transit time can greatly affect position reconstruction

	Average	Standard Deviation	Minimum	Maximum
Charge FWHM (pC)	1.42	0.4	1.18	2.32
Peak/Valley	2.8	0.28	2.3	3.0
High Charge tail (%)	2.86%	0.84%	2.5%	4.94%
Poisson Mean	0.015	0.006	0.011	0.025
Operating Voltage (V)	1848	75	1740	1920

Table 1: Summary of PMT SPE charge characteristics results for the R11780 standard quantum efficiency PMT. The operating voltage was adjusted to achieve a gain of 1×10^7 , which corresponds to a SPE charge peak of 1.6 pC. All measurements were made at room temperature.

	Average	Standard Deviation	Minimum	Maximum
Charge FWHM (pC)	1.64	0.62	1.19	3.36
Peak/Valley	2.24	0.27	1.78	2.76
High Charge tail (%)	3.75%	0.66%	2.73%	5.2%
Poisson Mean	0.023	0.005	0.015	0.029
Operating Voltage (V)	1950	221	1750	2500

Table 2: Summary of PMT SPE charge characteristics results for the R11780 high quantum efficiency PMT. The operating voltage was adjusted to achieve a gain of 1×10^7 , which corresponds to a SPE charge peak of 1.6 pC. All measurements were made at room temperature.

algorithms. A candidate PMT should therefore have a transit time spread that is as narrow as possible.

All coincident events taken from a typical data run are shown on the left side of Figure 7. For each event that has a hit in the Cherenkov source’s trigger PMT, we record a full 250 ns waveform for the R11780 being tested. The timing of this waveform is tied to the timing of the trigger PMT, which has a FWHM of just 250 ps and thus contributes a negligible additional jitter to the PMT timing profile. The waveform from the R11780 is broken into distinct regions and the total number of pulses in each region are counted if the charge integral of the pulse is greater than the electronic noise width. We define the time of a pulse as the time which the pulse amplitude crosses 20% of its peak height. We define a Δt for each pulse by subtracting the time of the peak of the pulse from the trigger PMT from the pulse time.

A typical Δt distribution is shown on the right in Figure 7. The timing distribution has several clear features: a nearly-Gaussian prompt peak, a broad feature attributed to late pulsing that peaks at roughly 75 ns, a continuum of late pulses between the prompt and the late pulsing peaks, a small peak attributed to pre-pulsing at around 30 ns before the prompt peak, and a uniform distribution of noise hits throughout the entire distribution. Late pulsing is caused by elastic scattering of photoelectrons off the first dynode, where they return later to the first dynode roughly two cathode-to-dynode transit times later. The continuum of late pulses is discussed in Section 4.5 and pre-pulses are caused when a photon passes through the glass and directly strikes the first dynode, and we define dark hits to be hits caused primarily by thermal electron emission from the photocathode and therefore are randomly distributed in time.

The timing parameters we have measured are:

- **Prompt Sigma:** Width of the prompt timing peak, measured by fitting a Gaussian in a ± 3 ns region around the maximum bin in the Δt distribution. The position

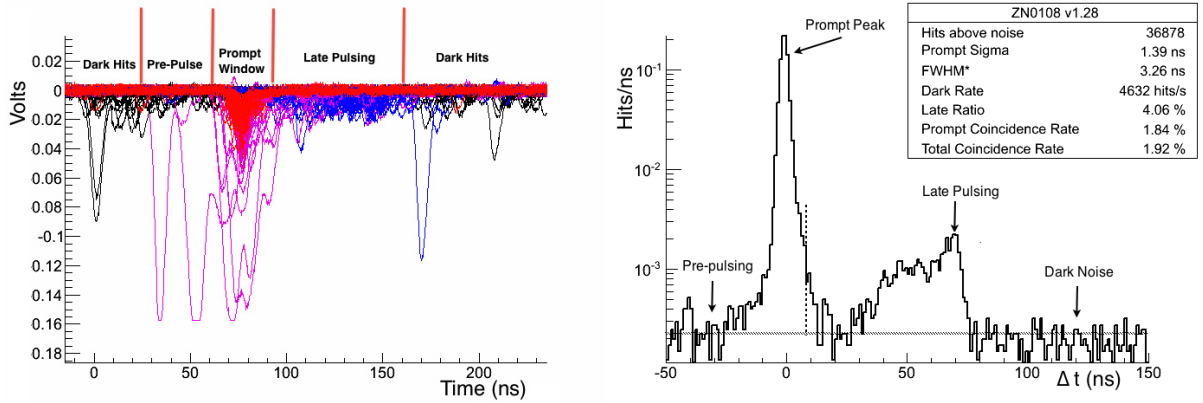


Figure 7: On the left, all traces with a coincident pulse from one individual data run are simultaneously plotted. The red color signifies traces that are within the prompt timing window. The magenta traces signify saturated pulses that were not used in the analysis because it was cut off by the limited dynamic range on the scope. The blue traces signify traces that fall within the late pulsing region, and finally the black traces indicate pulses that are either dark hits or pre-pulses. The right plot shows a typical Δt distribution with the different timing regions labeled.

resolution in a water Cherenkov detector depends on this parameter most directly.

FWHM: The FWHM value of the prompt peak is commonly called the ‘transit time spread’ (TTS) and is what PMT manufacturers specify. Assuming the shape of the prompt peak is described by a Gaussian, the FWHM is taken to be $2\sigma_{prompt}\sqrt{2\ln(2)}$.

Dark Rate: Rate of hits that that fall outside the prompt, the late pulsing, and the pre-pulsing regions.

Late Ratio: Fraction of hits in the late pulsing region. Dark hits are subtracted when calculating the ratio. The late pulsing region can be PMT-dependent, but we take this region to be from $5\sigma_{prompt}$ past the prompt peak to 80 ns after. Late pulsing is described in more detail in Section 4.5.

Prompt Coincidence Rate: Rate of prompt pulses (with the dark rate subtracted). To ensure the data for a given PMT is in the SPE regime, this value is kept below 5% for all tests.

Tables 3 and 4 show the results for our measurements of these parameters, for standard and high quantum efficiency versions of the R11780, respectively.

	Mean	Standard Deviation	Minimum	Maximum
Transit Time Spread (σ_{prompt}) (ns)	1.37	0.15	1.20	1.6
Late Pulses (fraction)	4.48%	0.32%	3.93%	4.92%
Noise Rate (Hz)	3669	5110	1962	16807
Operating Voltage (V)	1848	75	1740	1920

Table 3: Summary of PMT SPE timing characteristics results for the R11780 standard quantum efficiency PMT. The operating voltage was adjusted to achieve a gain of 1×10^7 , which corresponds to a SPE charge peak of 1.6 pC. All measurements were made at room temperature (20° C).

	Mean	Standard Deviation	Minimum	Maximum
Transit Time Spread (σ_{prompt}) (ns)	1.29	0.14	1.16	1.52
Late Pulses (fraction)	4.3%	0.35%	3.6%	4.8%
Noise Rate (Hz)	4428	1897	2398	8217
Operating Voltage (V)	1950	221	1750	2500

Table 4: Summary of PMT SPE timing characteristics results for the R11780 high quantum efficiency PMT. The operating voltage was adjusted to achieve a gain of 1×10^7 , which corresponds to a SPE charge peak of 1.6 pC. All measurements were made at room temperature (20° C).

As the tables show, both tubes have outstanding timing resolution, making precision reconstruction in very large detectors possible. Their TTS is substantially better than both the PMTs used in the Super-Kamiokande and SNO detectors [18, 1]. The higher dark noise rate in the HQE PMTs is not surprising, given their overall higher quantum efficiency.

4.3. Relative Quantum Efficiencies of R11780 Configurations

The single photoelectron response of the standard QE and HQE PMTs are similar and are both very good. To estimate the overall gain in quantum efficiency of the HQE configuration compared to the standard version, we tested the relative quantum efficiency of the HQE configuration compared to the standard QE PMT by running both tube configurations triggering off the same Cherenkov source. Although the overall particle detection efficiency of a PMT is the product of the quantum efficiency response with its collection efficiency, the ratio of the coincidence rates provides an accurate measure of the relative quantum efficiency since the PMT collection efficiency is the same for both tube configurations. We compared the relative efficiencies of six HQE tubes to six standard QE tubes. Hamamatsu anticipated about a 52% average increase in quantum efficiency between the HQE and standard QE configurations at 390 nm. Using the relative coincidence rates as a measure of the relative quantum efficiencies, we find that the relative quantum efficiency of the HQE version of the tube is on average 50% higher than the standard quantum efficiency version as shown in Table 5. These results are consistent with Hamamatsu’s projections, however, the light which triggered the tested PMTs exhibited a broadband wavelength spectrum. Hamamatsu large-area PMTs are typically sensitive in the approximately 300-600 nm range. The 15% standard deviation in the relative efficiency is dominated by two outlying PMTs. These outlying PMTs only demonstrated a 32% improvement over the standard tubes. The results of these outlying PMTs could mean either that these particular HQE tubes have a lower peak quantum efficiency than the expected 32%, or that the particular standard tubes used for the relative comparison have a higher peak quantum efficiency than the expected value of 21%. Further testing of larger samples of PMTs could settle this.

4.4. Absolute Measurement of the R11780 Particle Detection Efficiency

The particle detection efficiency (PDE) of one 12” R11780 standard QE PMT was measured. The absolute quantum efficiency is expected to be around 21% at a wavelength of 390 nm. The measured particle detection efficiency is less than the absolute quantum efficiency since collection efficiency is not 100% due to photoelectrons missing the first dynode and inelastic back scattering of photoelectrons off the first dynode. A

	Relative Efficiency
Tested Pair 1	1.56
Tested Pair 2	1.49
Tested Pair 3	1.66
Tested Pair 4	1.64
Tested Pair 5	1.32
Tested Pair 6	1.32
Average	1.50
Standard Deviation	0.15

Table 5: Observed relative efficiency of the high quantum efficiency configuration of the R11780 PMT compared to the standard quantum efficiency configuration. The relative efficiencies were measured using the relative coincidence rates, which is a reasonable metric for a pure single photoelectron source.

DC deuterium lamp was focused into a monochromator. A filter wheel and a 2" integrating sphere were mounted on the monochromator output. The filter wheel contained a neutral density filter, with reduction factor of roughly 250, a dark frame, and several open positions. A 1 mm UV/VIS optical fiber was mounted in one port of the integrating sphere, carrying the light to a dark box. A monitoring photodiode was mounted in a second integrating sphere port. The current from the photodiode was measured using a pico-ammeter.

A NIST calibrated photodiode in the dark box was used to determine the absolute photon flux emitted by the optical fiber. The low light level required for single photon QE measurement is insufficient to drive this photodiode significantly above its thermal output, so calibration of fiber emission was done at higher light levels. The geometry of the integrating sphere ports and coupling to the fiber were arranged such that with the filter wheel in the open position the output of the monitoring photodiode was well up in its operating range, while that for the calibrated photodiode was near its minimum of a few 10s of pA. The monochromator was scanned in 10 nm steps through wavelengths between 290 and 500 nm, and the outputs of both photodiodes were recorded in separate pico-ammeters.

We then selected the NDF position of the filter wheel, reducing the light by a factor of 250, and relied on the linearity of the wide dynamic range of the monitoring photodiode output to provide the reduction factor for calculation of the fiber emission relative to that measured in the open filter wheel position. Although the NDF is wavelength dependent, both the integration sphere and the NIST calibrated photodiode are downstream of the NDF and therefore any wavelength dependence does not affect the correlation between the integrating sphere response and the NIST photodiode output. The equivalent output of the NIST-calibrated photodiode with the NDF in place, if directly measurable, would be on the fA scale, corresponding to a few kHz of photons from the fiber end.

The PMT was placed into our dark box with the end of the optical fiber centered on the photocathode, illuminating a spot of approximately 5 mm². A voltage of 1850V was applied to the base, corresponding to the HV used for this tube during the charge and timing tests described above. The output was connected to a fast Ortec x10 preamp. The signal then went to a discriminator with a threshold set at -400 mV. The number of pulses below -400 mV were counted for a period of 10 seconds. We varied the threshold on the discriminator and found that the background subtracted rate from the PMT was insensitive to variations. We also looked at the raw traces from the PMT on an

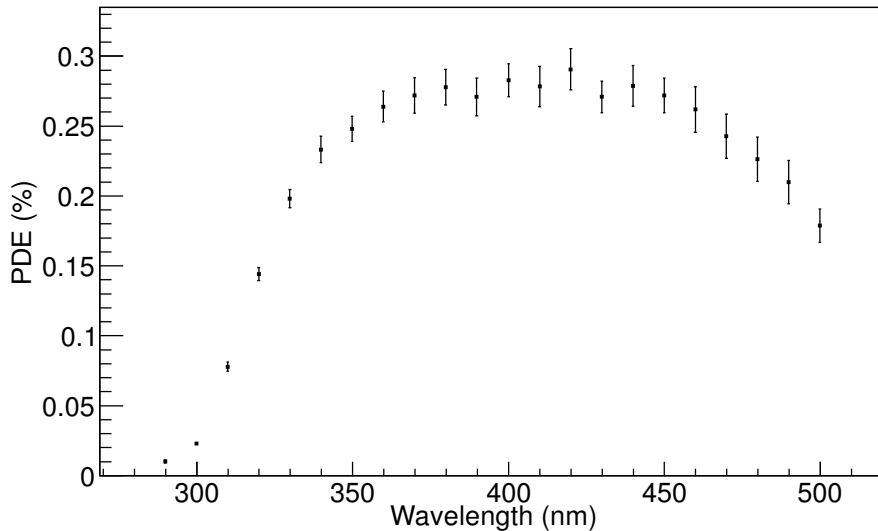


Figure 8: The measured particle detection efficiency of the 12" R11780 PMT with standard quantum efficiency.

oscilloscope and observed that the real photon hits were much larger than -400 mV. The response of the PMT was measured from 290 nm to 500 nm in 10 nm steps. At each wavelength five dark rate and signal rate counts were recorded to insure stability, these were then averaged and the *signal - dark* rate for each wavelength was recorded for each wavelength. The background subtracted rate was typically several kHz.

We then took the background subtracted rates and divided them by the absolute photon flux for each wavelength, giving the PMT quantum efficiency, shown in the plot below. The uncertainties are calculated using the one sigma deviation of all averaged quantities added in quadrature, including the currents from the two photodiodes and the hit rates measured from the PMT. The errors vary from 10% below 300nm to 3-5% for the rest of the wavelengths, the higher uncertainty at 290nm is due to a low photon flux at this wavelength. The uncertainty in the NIST absolute calibration of the reference photodiode is less than 1% in this wavelength range.

We note that the peak PDE of this small spot at the center of the photocathode of the tested R11780 standard QE PMT is near 28%, which is significantly higher than the anticipated PDE averaged over the full photocathode. It is to be expected that the collection efficiency at the center of the photocathode is significantly higher than when averaged over the entire photocathode surface. It is also higher than the 25% average absolute QE of the 10-inch R7081 PMT. Fluctuations in the relative response over the photocathode have been measured (see Figs. 13 and 14), and this is one possible explanation. Alternatively, the measured PDE can be dependent on the experimental geometry and can include effects of light backscattered from the internal reflective surfaces of the PMT to the photocathode and the photon-photocathode angle of incidence. The angle of incidence is of particular relevance for PMTs with a curved face. In addition, we measure the PDE at a small spot at the center of the photocathode, which differs from the technique used by the manufacturer and is intended for use in evaluating an effective PDE in conjunction with full photocathode scans as shown in Figs. 13 and 14. Finally, this measurement of the particle detection efficiency may suggest that there are large tube-to-

tube variations in the peak quantum efficiency in the initial sample of R11780 standard QE tubes manufactured by Hamamatsu, with a few tubes including the tested PMT in Figure 8 exhibiting larger than anticipated peak quantum efficiency. This conclusion is also supported by the data in Table 5 since one of the outlying HQE tubes that exhibited a lower than anticipated relative efficiency of 32% over a standard QE tube was in fact compared to the standard QE tube measured in this section.

4.5. Late Pulsing and Double Pulsing

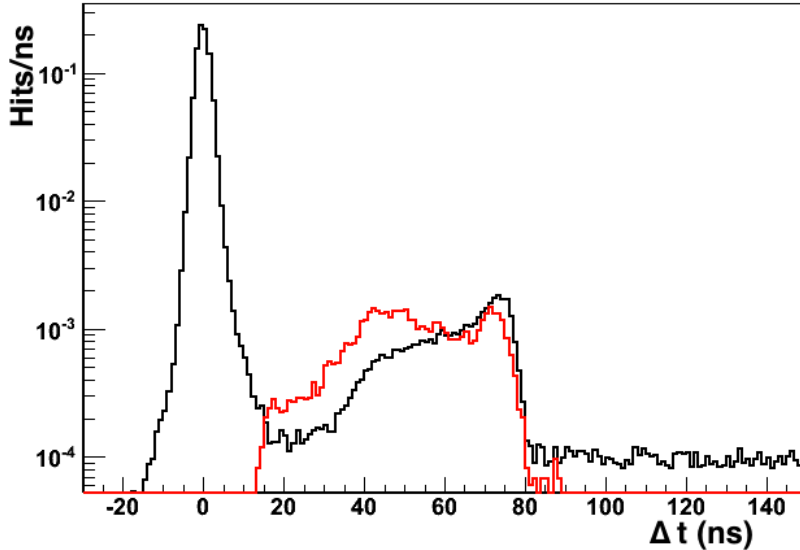


Figure 9: A high statistics transit time distribution for a 12'' R11780 PMT with high quantum efficiency. The times of the second pulses in double pulse triggers are shown by the dotted red curve.

As was discussed in Section 4.2, there is a clear peak near 75 ns in the transit time spread distribution. This ‘late pulsing’ peak is caused by elastic scattering of photoelectrons off of the first dynode. After scattering, the photoelectrons return to the first dynode roughly two cathode-to-dynode transit times later. There is a related phenomenon known as double pulsing, which is caused by inelastic scattering off of the first dynode. The inelastic scatter results in a prompt pulse followed by a second pulse. This second pulse arrives earlier than is typical for a late pulse because of the energy lost by the photoelectron due to the scattering. This second pulse could also be due to ‘fast afterpulsing’, pulses that arise from light emission from the dynodes themselves, though the time scale of such pulses are typically earlier than the late pulses and double pulses. Figure 9 shows the transit time spread distribution comparing the timing profile of a second pulse in double-pulse triggered events to the late pulsing distribution for a R11780 HQE tube. Such characterization of this behavior can be used in algorithms that estimate the number of detected photoelectrons, or in reconstruction algorithms to ensure that a double pulse event is not counted as two photons.

4.6. PMT Position-Dependent Response

The charge and time observables measured in the SPE characterization don’t convey any information about the direction of the incident photon or where it struck the

photocathode. The optics of the glass and the transmission and absorption of the semi-conducting photocathode layer can lead to an angular dependence of the photon detection efficiency. The position-dependent response can in principle be wavelength-dependent, especially for ultraviolet photons which can impart enough transverse momentum to miss the first dynode. The thickness of the PMT glass for the 12-inch tube however, is enough to absorb most UV photons. Optical models of the photocathode layer have been successfully created based on measurements of the complex index of refraction of the photocathode material. Along with optical models of the PMT glass, these models provide good predictions for the PMT angular response [18, 14]. Such models have been used both in PMT simulations and in reconstruction algorithms [22].

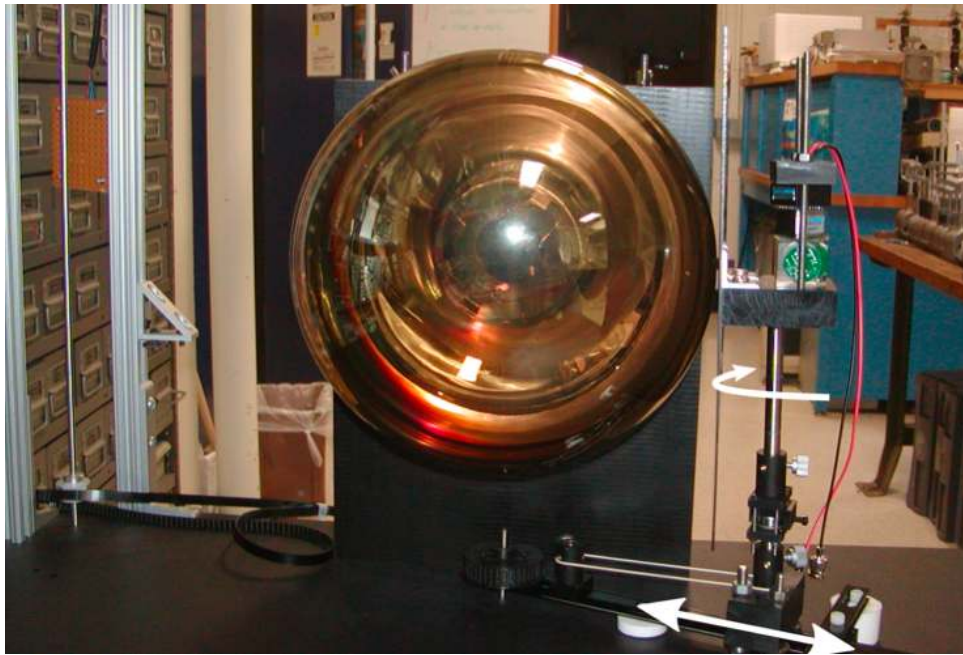


Figure 10: The scanning arm setup used to test the angular dependence of the single photoelectron response of the Hamamatsu R11780 PMT.

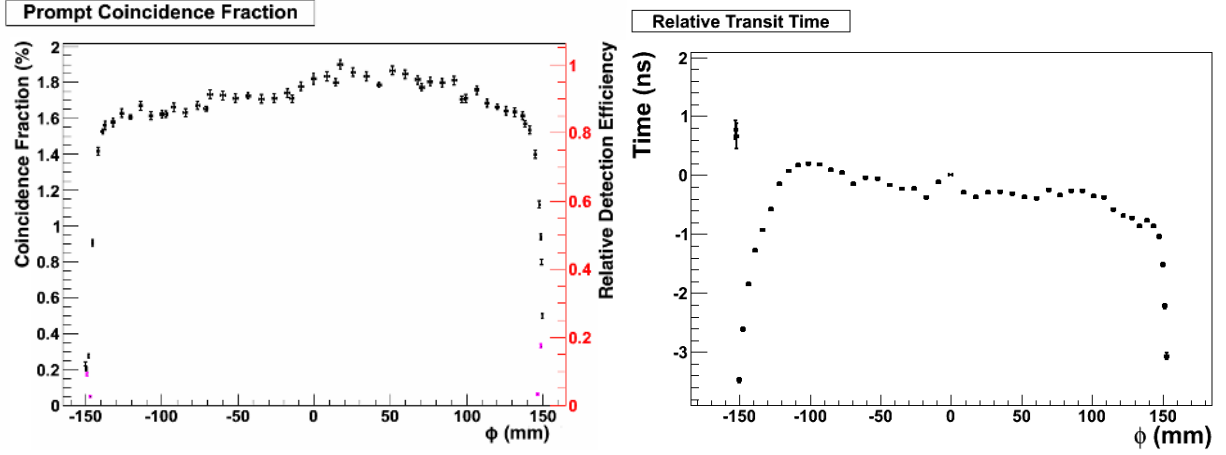


Figure 11: A one-dimensional scan of the coincidence fraction and relative detection efficiency along the diameter of the PMT is shown on the left, while position dependent shifts along the diameter in the relative transit time is shown on the right. The scans were made for a Hamamatsu 12-inch R11780 PMT with standard quantum efficiency.

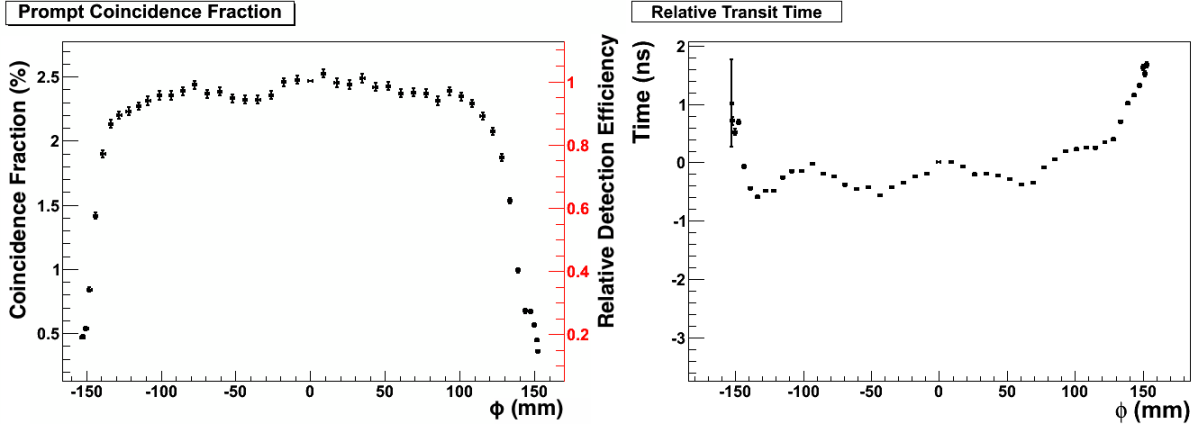


Figure 12: A one-dimensional scan of the coincidence fraction and relative detection efficiency along the diameter of the Hamamatsu 12-inch R11780 high quantum efficiency PMT is shown on the left, while position dependent shifts along the diameter in the relative transit time is shown on the right. The scanned high quantum efficiency PMT has an alternative dynode structure designed to mitigate the large shifts in the mean transit observed in the standard configuration shown in Figure 13.

Beyond the angular dependence, however, there is the possibility of a position dependence of the photon detection efficiency or to the overall transit time of a created photoelectron along the photocathode. Such a dependence can be due to non-uniformities of the photocathode layer itself or due to variations in the electron optics from the photocathode to the first dynode. The electron optics can especially affect the position dependence in the observed transit time. The reflective surface within the PMT glass could also affect the position-dependence, however a simulation of the photoelectron response reveals that the impact of the reflective surface on the position-dependence is minor. A full model of a PMT photon detection efficiency would thus include the wavelength-dependence of the quantum efficiency, the angular-dependence of the efficiency due to the optics of the glass and photocathode, and any position-dependence of the photon detection efficiency and the transit time. Although large variations across the surface of the photocathode can in principle be included in a complete optical model, such large deviations are not

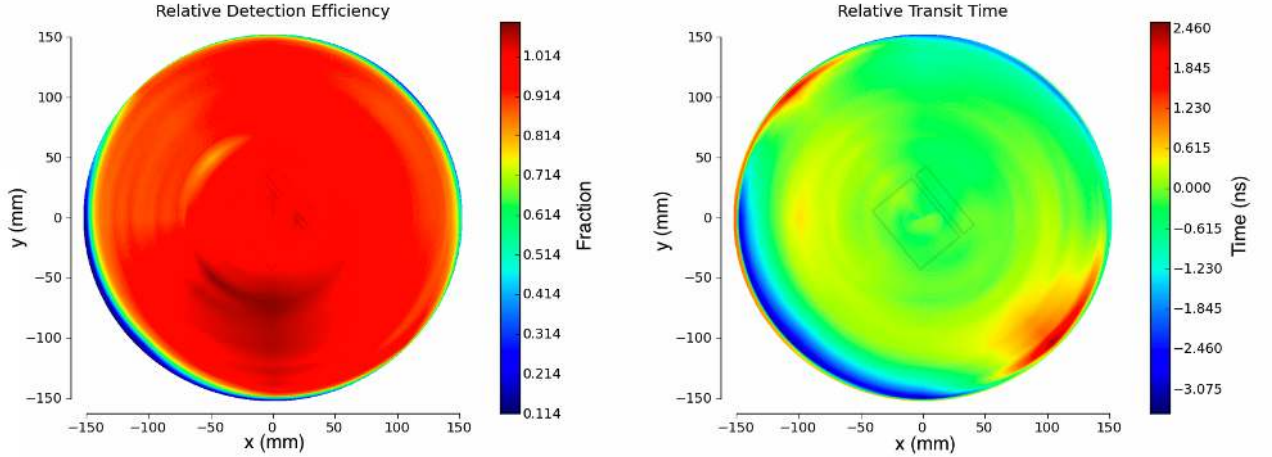


Figure 13: The position-dependent photon detection efficiency is shown on the left, while position dependent shifts in the median transit time is shown on the right for a Hamamatsu 12-inch R11780 PMT with standard quantum efficiency. The color indexes are relative to measurements made at the center of the PMT.

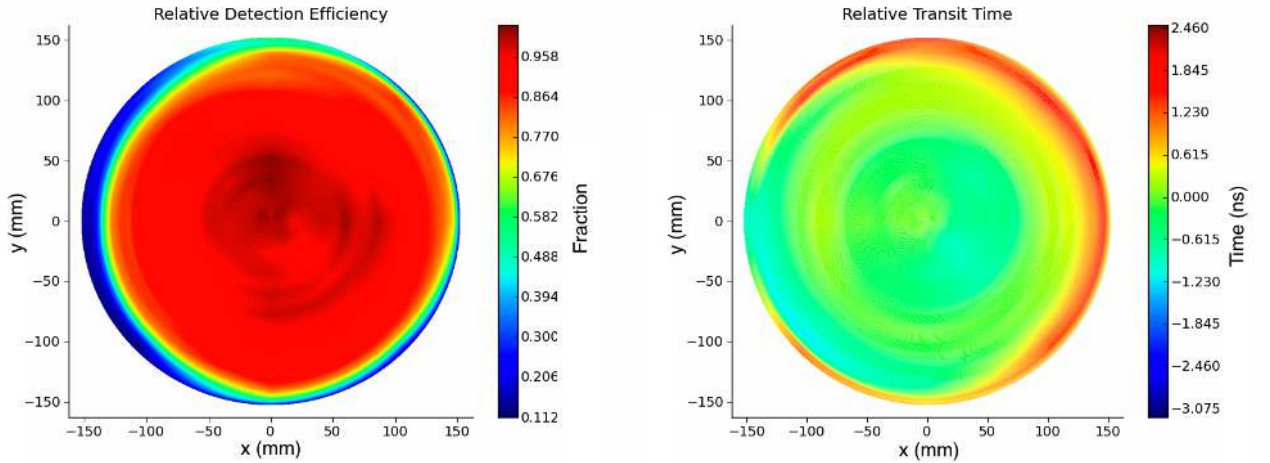


Figure 14: The position-dependent photon detection efficiency is shown on the left, while position dependent shifts in the median transit time is shown on the right for the high quantum efficiency configuration of the Hamamatsu 12-inch R11780 PMT. The scanned high quantum efficiency PMT has an alternative dynode structure designed by Hamamatsu to mitigate the large shifts in the mean transit time observed in the standard configuration shown in Figure 13. The color indexes are relative to measurements made at the center of the PMT.

desired and therefore we perform the measurement to characterize the uniformity of the R11780 PMT.

To measure position-dependence of timing and detection efficiency for the R11780, we constructed a scanning arm that placed our Cherenkov source at normal incidence to the PMT face, as shown in Figure 10. To ensure we remained in the single photoelectron regime, a pinhole mask was used to block most of the light except for a pinhole with a diameter of roughly 3 mm. The position of the source was varied by mounting the light source, a mask, and the trigger PMT on an optical rail with its pivot point just below the center of the test PMT. The entire mounted setup was controlled by a stepper motor that was operated remotely. The PMT was mounted at its neck onto a large plastic

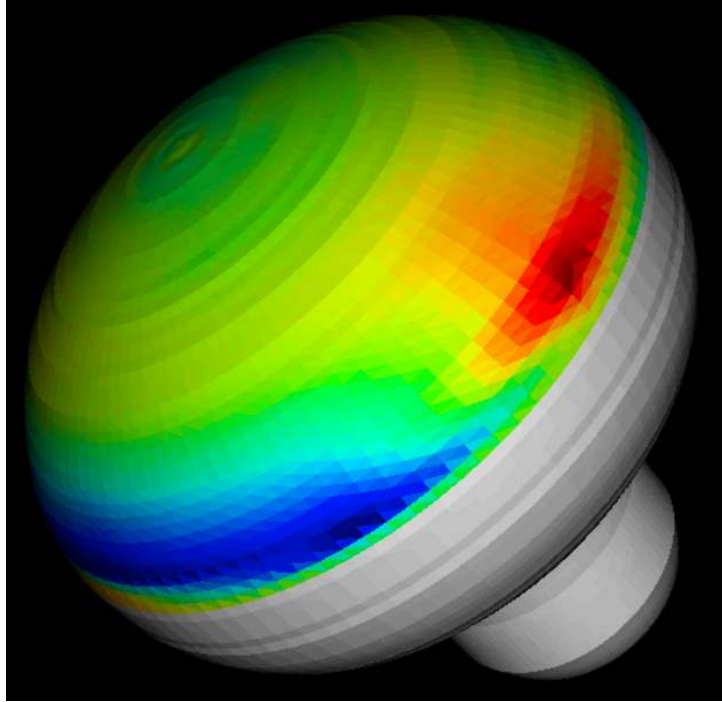


Figure 15: The position dependent shifts in the median transit time from Figure 13 is superimposed on a 3d model of the R11780 PMT to demonstrate the size of the regions with large shifts in the median transit time. The color indexes are relative to measurements made at the center of the PMT.

sheet which itself was mounted onto the optical rail to ensure proper alignment of source and PMT. We scanned the source across the face of the PMT using 50 points across the full diameter, and then rotated the PMT by 45 degrees between scans. A total of four diameter scans were performed.

The results of the measurements for a standard quantum efficiency R11780 are shown in Figures 11 and 13. For the two-dimensional map, we interpolated along the arc between measurements to produce the contours. In Figure 15 we show the timing shift map superimposed on a 3D model of the R11780 to better illustrate the size of the early-shifted region.

As the figures show, the efficiency of the R11780 is very uniform across the photocathode, with the exception of the region beyond about 135 mm where it begins to drop off. The majority of this region is outside the area that Hamamatsu specifies for these PMTs. There is a clear asymmetry in the lower-efficiency region, which appears to be aligned with the first dynode of the PMT, indicating that the drop off is more likely caused by electron optics than a non-uniformity in the photocathode itself.

We also see in the figures that there are large shifts that are noticeably larger than the transit time spread in the mean transit time as one gets toward the edge of the PMT. These shifts also appear to be aligned with the dynode structure, and Hamamatsu has confirmed that their electron optics simulation [23] reproduces these shifts. Hamamatsu produced a prototype sample of five R11780 high quantum efficiency tubes with an alternative dynode structure designed to mitigate the transit time shifts near the edge of the PMT. The resulting scans across the PMT surface for one of the new HQE tubes are shown in Figure 12 and Figure 14. We note that the large shifts in the relative transit time observed near the edge of the standard quantum efficiency tube are significantly

reduced in the new high quantum efficiency configuration with the alternative dynode structure. The cost of the improved timing uniformity is a larger region of decreased photon detection efficiency as shown in the left plot of Figure 14. We finally note that the position dependence of the efficiency and the transit time for the new HQE configuration below the region of about 135 mm is extremely similar to the standard quantum efficiency configuration.

4.7. Multiple Photon Contamination

The results reported in this paper would ideally measure the response of the R11780 PMT to single photons incident to the photocathode. For an isotropic light source, fluctuations in the number of photons detected by a PMT follow a Poisson distribution and can thus be calculated exactly. For our source, however, the angular distribution of Cherenkov light and the broad energy spectrum of the ^{90}Sr β source mean the multi-photon contamination is much higher. Multiple scattering of the β within the acrylic mitigates this effect somewhat by making the distribution much more isotropic than a canonical Cherenkov cone, but nevertheless these additional photons do contaminate our single photoelectron sample.

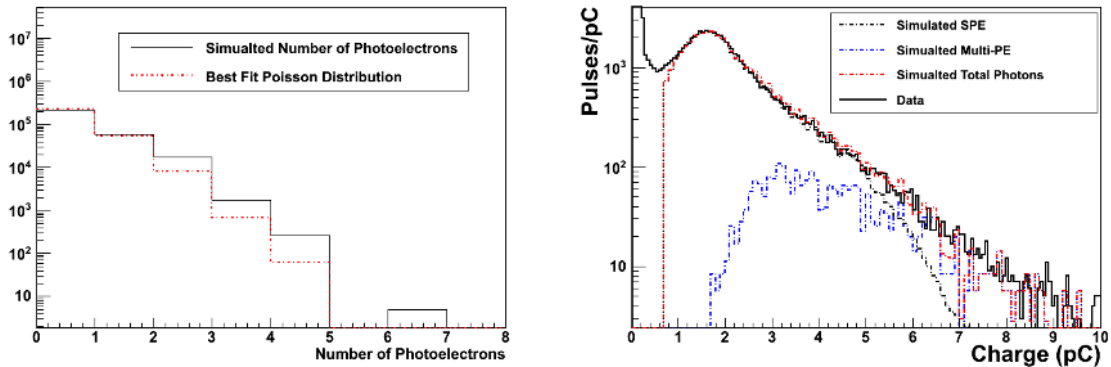


Figure 16: The left plot shows the distribution of detected number of photoelectrons as predicted by simulation. A Poisson distribution was fit to the photoelectron distribution and is also shown. The simulation was performed using the Reactor Analysis Tool (RAT) software. The right plot shows the measured single photoelectron charge spectrum for a R11780 high quantum efficiency PMT compared with the simulated single photoelectron charge spectrum along with the predicted multiple photon contamination. The simulation predicts that multiple photons contribute 6.5% to the total number of pulses, in comparison to a 3% contribution from a Poisson distribution. The Monte Carlo simulation does not include the effects of afterpulsing, since after pulsing is PMT specific and can not be accurately predicted.

Detected photons	Simulated % of total	Poisson % of total	Simulation / Poisson
2 or more	6.5%	3%	2.2
2	5.8%	2.7%	2.15
3	0.67%	0.23%	2.5
4	0.087%	0.021%	4.1

Table 6: The multiple-photon contamination contribution from the simulation and a Poisson distribution is tabulated for various numbers of detected photons. The simulation was performed using the RAT software. The Poisson distribution was taken from a fit to the simulated photoelectron distribution in the left plot of Figure 16.

To estimate the level of multi-photon contamination, we developed a Monte Carlo simulation of the SPE characterization experimental setup using the RAT [24] framework, which is used for the simulation of the SNO+ and MiniCLEAN experiments. The Monte Carlo simulation incorporated a full description of the geometry, optics, timing, and quantum efficiency response of the R11780 PMT. The single photoelectron response for the R11780 implemented in the simulation was taken from the measured data. A high statistics Monte Carlo simulation of two million events was generated in order to estimate the contribution of two or more incident photons on the simulated charge spectrum for the R11780 12-inch PMT. The simulated number of detected photoelectrons is compared to a fit of a Poisson distribution to the photoelectron spectrum on the left plot of Figure 16. The simulated multi-photon contribution from two or more detected photoelectrons is 6.5% of the total number of photoelectrons, which is higher compared to the Poisson contribution of 3%. The detected multiple-photon contamination from simulation and a Poisson distribution is tabulated in Table 6 for different multiplicities of detected photons. We note that the deviation of the simulation from the Poisson prediction increases for higher multiplicities of detected photoelectrons.

The resulting simulated charge spectrum is compared to data on the right plot of Figure 16. The simulation predicted that 6.5% of all simulated pulses arose from multiple-photon events, which is compatible with the measured high-charge tail of the SPE charge distribution. We note the possibility of bias in the right plot of Figure 16 since the simulated single photoelectron response is taken from the data, which is known to have contamination from multiple photoelectrons. However, the simulation shows that the charge distribution arising from the contribution of multiple photons is well away from the single photoelectron peak and shows up predominately in the high charge tail.

Our simulation has shown that the chosen SPE characterization parameters, with the exception of the high charge tail, are insensitive to the multi photon contamination. So although our Cherenkov source is not a pure Poisson source, the amount of contamination is acceptable for the SPE characterization and our parameters are indicative of the true SPE response.

5. Conclusions

The 12" R11780 PMT from Hamamatsu is an excellent candidate PMT for very large-scale water Cherenkov or scintillator detectors. The SPE charge and timing response are excellent, and the high quantum efficiency version is a cost-effective solution that increases the detected photon yield on average by about 50%. A two-dimensional scan of the standard quantum efficiency version of the R11780 PMT revealed that the charge and timing response is uniform across most of the photocathode surface, although there are noticeable timing shifts near the edge of the PMT. Further research and development work by Hamamatsu resulted in an alternative dynode structure designed to resolve the problem. A two-dimensional scan of the high quantum efficiency version of the R11780 PMT with the alternative dynode structure revealed that the observed timing shifts have been mitigated. Finally, a simulation of the single photoelectron experimental setup shows that contamination from multiple photons is relatively small and therefore the results reported here are indicative of the true SPE response of the Hamamatsu R11780 PMT.

Acknowledgments

We acknowledge the support from the following agencies:
U.S. National Science Foundation-Physics Division,
U.S. Department of Energy

- [1] Y. Fukuda, et al., Nuclear Instrumentation and Methods A 501 (2003) 418.
- [2] The SNO Collaboration, Phys. Rev. Lett. 87 (2001) 071301.
- [3] The RENO Collaboration, Phys. Rev. Lett. 108 (2012) 191802.
- [4] The Daya Bay Collaboration, Phys. Rev. Lett. 108 (2012) 171803.
- [5] The LBNE collaboration, Long-baseline neutrino experiment collaboration conceptual design report, <http://lbne.fnal.gov/reviews/CD1-CDR.shtml> (2012).
- [6] M. Wurm, et al., The next-generation liquid-scintillator neutrino observatory lena, arXiv:1104.5620.
- [7] K. Abe, et al., Letter of intent: The hyper-kamiokande experiment, arXiv:1109.3262.
- [8] The IceCube Collaboration, Astroparticle Physics 35 (2012) 615.
- [9] J. F. Beacom, M. R. Vagins, Phys. Rev. Lett 93 (2003) 171101.
- [10] A. Baltz, J. Weneser, Phys. Rev. D. 51 (1995) 3960.
- [11] The SNO+ collaboration, The sno+ experiment, arXiv:08:10.3694.
- [12] The KamLAND-Zen collaboration, Phys. Rev. C. 85 (2012) 045504.
- [13] A. Achterberg, et al., First year performance of the icecube neutrino telescope, Nuclear Instrumentation and Methods A 618 (2010) 139–152.
- [14] A. Abbasi, et al., Calibration and characterization of the icecube photomultiplier tube, Astropart. Physics 26 (2006) 155, arXiv:1002.2442.
- [15] A. Hime, The miniclean dark matter experiment, arXiv:1110.1005.
- [16] The LBNE collaboration, Long-baseline neutrino experiment water cherenkov conceptual design report, arXiv:1204.2295v1 (2012).
- [17] Hamamatsu Photonics, PMT Handbook, sales.hamamatsu.com/en/support/application-notes.php.
- [18] The SNO Collaboration, The sudbury neutrino observatory, Nuclear Instrumentation and Methods A 449 (2000) 172–207.
- [19] A. Latorre, <https://bitbucket.org/tlatorre/lecrunch/>.
- [20] Hitachi Metals, Ltd., <http://www.hitachi-metals.co.jp/e/prod/prod02/pdf/hl-fm10-d.pdf>.
- [21] http://notdirac.hep.upenn.edu:5985/pmt-v1-28/_design/DB-update/_list/specific_tube/overview?reduce=true&group
- [22] M. Dunford, Measurement of the $(8)\text{b}$ solar neutrino energy spectrum at the sudbury neutrino observatory, Ph.D. thesis, University of Pennsylvania.
- [23] Hamamatsu Photonics, private communication (2011).
- [24] S. Seibert, et al., Rat, , <http://nu.ph.utexas.edu/rat/trac>.